Marine Boundary Layer Cloud Observations at the Azores

Jasmine Rémillard[1], Pavlos Kollias[1], Edward Luke[2] and Robert Wood[3]

1. Department of Atmospheric and Oceanic Sciences, McGill University, Montreal QC
2. Atmospheric Sciences Division, Brookhaven National Laboratory, Upton NY
3. Department of Atmospheric Sciences, University of Washington, Seattle WA

Corresponding Author's email: jasmine.remillard@mail.mcgill.ca
Department of Atmospheric and Oceanic Sciences
Room 945, Burnside Hall, 805 Sherbrooke Street West
Montreal, Quebec H3A 2K6
Tel.: 514-398-1500
Fax: 514-398-6115

Abstract

The recent deployment of the ARM Mobile Facility at the Graciosa Island, Azores in the context of the Clouds, Aerosol and Precipitation in the Marine Boundary Layer (CAP-MBL) field campaign added the most extensive and comprehensive dataset of MBL clouds to date (April 2009–December 2010). Cloud occurrence is high (60–80%) with a summertime minimum. Liquid precipitation, diagnosed as the detection of hydrometeors below the cloud base, is frequently present (30–40%), mainly in the form of virga. MBL clouds are the most frequently observed cloud type (40–50%) with a maximum of occurrence during the summer and fall months under the presence of anticyclonic conditions. Cumulus clouds are the most frequently occurring MBL cloud type (20%), with cumulus under stratocumulus layers (10–30%) and single-layer stratocumulus (0–10%) following in frequency of occurrence. The presence of a stable transition layer in the subcloud layer is detectable in the vast majority of the radiosondes (92%) with MBL clouds. Cumulus cloud bases and stratocumulus cloud tops correlate very well with the top of the transition layer and the inversion base respectively. Drizzling stratocumulus layers are thicker (350–400 m) and have higher liquid water path (75–150 gm^{-2}) than their non-drizzling counterparts (100–250 m and 30–75 gm^{-2} respectively). The variance of the vertical air motion is maximum near the cloud base and is higher at night. The updraft mass flux is around 0.17 $kgm^{-2}s^{-1}$ and coherent updraft structures explain 40–60% of the mass flux. The observations demonstrate that the MBL is almost never well mixed and is often cumulus-coupled.

1. INTRODUCTION

Marine stratocumulus clouds are ubiquitous over the eastern the subtropical oceans and play a critical role in the boundary layer dynamics and the global climate (e.g., Klein and Hartmann, 1993; Bony and Dufresne, 2005). These prevailing low-level cloud decks are a key component in Earth's radiation budget (Randall et al., 1984; Ramanathan et al., 1989). The radiative impact of marine boundary layer clouds depends on their macroscopic properties (e.g., horizontal extent, thickness) and microscopic properties (e.g., particle size distribution). Past studies have focused on the cloud macro-structure properties of marine boundary layer clouds (e.g., Klein and Hartmann, 1993) and their relationship to large-scale dynamics and thermodynamic state using satellite observations and reanalysis products. Recently, Wood and Bretherton (2006), have shown that approximately 80% of the variance in low cloud cover in regions dominated by marine stratocumulus is explained using the estimated inversion strength. However, appreciable complexity and challenges are found on smaller space and time scales, including the cloud micro-scale.

Previous field experiments focusing include the Atlantic Stratocumulus Transition Experiment–ASTEX (Albrecht et al., 1995), the East Pacific Investigation of Climate–EPIC (Bretherton et al., 2004), the Dynamics and chemistry of marine stratocumulus–DYCOMS (Stevens et al., 2003) and the VAMOS Ocean-Cloud-Atmosphere-Land Study Regional Experiment–VOCALS-REx (Wood et al., 2011). The abovementioned field studies advanced our knowledge of marine stratocumulus providing information on the boundary layer thermodynamic and cloud structure, as well as their diurnal cycle. They have highlighted that stratocumulus clouds can form under a diverse range of conditions, in both deep and shallow marine boundary layers (MBL), and under a wide range of aerosol conditions. These clouds radiative and precipitation properties are sensitive to aerosols, liquid content, cloud depth, and insolation.

However, despite their extreme usefulness, these field experiments were limited in time. They have not been carried long enough to provide a useful climatology of key properties. The recent Clouds, Aerosol and Precipitation in the Marine Boundary Layer

(CAP-MBL) field campaign (www.arm.gov/sites/amf/grw/) that took place in the Azores nicely filled that gap. As part of it, the US Department of Energy Atmospheric Radiation Measurements (ARM) Mobile Facility (AMF) was deployed at the Graciosa Island. This AMF deployment is unique compared to previous intensive field campaigns. First, the AMF instrumentation is far more comprehensive and superior to that available in previous ground-based field studies. Second, the campaign is 21 months long and thus provides the opportunity to generate the long data set record required to sample a variety of aerosol, cloud and large-scale environmental conditions. Finally, it is the first marine stratocumulus field campaign with sophisticated cloud radars (profiling and scanning) on a stable (island) platform that enables the use of the Doppler velocity measurements. Thus, the AMF deployment at Azores produced the most comprehensive data set of MBL clouds to date.

In this study, we select a subset of the deployed AMF instruments to study the observed MBL clouds in more detail. An objective scheme was first developed to identify their occurrence across the entire data set, and to recognize some important subtypes (e.g., cumulus and stratocumulus), with the presence of precipitation also diagnosed (see section 3). A climatology of different types of cloud is thus formed, focusing on various MBL cloud structures. A further analysis of the MBL emphasizes the differentiation between cumulus and stratocumulus regimes, as well as the presence of decoupling. A statistical analysis of cloud structural and dynamical properties is performed, and related to the thermodynamic profiles.

2. OBSERVATIONS

The CAP-MBL field campaign lasted 21 months (April 2009 to December 2010), permitting the sampling of almost two full years of cloud and precipitation conditions at Azores. Although this location has been used in the past for the study of marine stratocumulus clouds (ASTEX), a variety of cloud conditions were sampled which include shallow cumulus, cumulus under stratocumulus, deeper convection and frontal systems. The AMF with its usual comprehensive array of aerosol, cloud, precipitation

and radiation sensors was deployed near the north shore of Graciosa Island (39.09°N, 28.03°W, include altitude AMSL). This location is upwind of the climatological wind conditions in the MBL and was selected to reduce the island effect. The primary instruments used in this study to describe the cloud and precipitation conditions are: a W-band (95-GHz) Doppler radar, a laser ceilometer, a two-channel microwave radiometer and radiosondes (four per day). The instruments were placed within a few meters of each other; thus, to the extent possible their measurements describe the same atmospheric column. The operational status of the three remote sensors is summarized in Fig. 1, allowing gaps of up to one minute to be considered within normal operation. Overall, the observations are fairly continuous with great overlap between the three remote sensors, spatially as well as temporally.

2.1 W-band Doppler radar

A baseline instrument of the AMF is the W-band ARM Cloud Radar (WACR; Mead and Widener, 2005), a 95-GHz vertically pointing Doppler radar. Millimeter wavelength radars are ideally suited for the study of MBL clouds (e.g., Kollias et al., 2007a). Due to its short wavelength (3.15 mm), it is sensitive enough to detect cloud droplets (-50 dBZ at 2 km), while attenuation is small in light to moderate drizzle conditions. Furthermore, it uses a beam width narrow enough (0.19°) to provide high temporal and spatial resolutions (respectively around 2 s and 43 m). Its primary measurement is the Doppler spectrum, reporting the full distribution of the returned radar echo over the range of sampled Doppler velocities. Thus, detailed information about cloud microphysics and dynamics are inherent in the radar measurements (e.g., Kollias et al., 2011a; Luke et al., 2010). The WACR also provides an estimate of hydrometeor (i.e., cloud and drizzle) boundaries (see section 3.1 below), as it is only sensitive to these atmospheric particles. However, some parts of non-precipitating liquid clouds might be missed if the cloud droplets are not large enough. For the Azores deployment, the WACR began operating on the morning of June 5th, 2009, and operated until the end of the campaign. One major interruption occurred in September 2010, when the radar was down for almost 23 days,

due to a hard disk problem. Otherwise, the radar experienced six downtimes of more than an hour (including three extending over about 1.5 day), and a few shorter, for a total of less than 10% of a month (see Fig. 1, black bars). Note also that the radar used alternating co- (H-H) and cross-polarized (H-V) operating modes through late 2009, when it began operating continuously in co-polarized mode. The cross-polarized measurements are not used here, since MBL clouds have spherical cloud and drizzle particles. Therefore, the time between profiles is around 4 s for the earlier months, and 2 s for the latter. Nonetheless, given the horizontal scales of the sampled clouds the results should not be affected by that change.

2.2 Ceilometer

Another baseline AMF instrument is a Vaisala ceilometer (CT25K model, upgraded in mid-July 2010 to the CL31 model; Münkel et al., 2007), a near-infrared vertically pointing lidar. It provides profiles of the atmospheric column mainly up to the liquid cloud base, as cloud droplets prevent in-cloud measurements by extinguishing the laser signal. Nevertheless, the sharp increase and subsequent decrease of the lidar backscatter at the level of the cloud base is very useful for deriving the actual cloud base height, while still being able to profile drizzle and aerosols particles under the cloud (e.g., O'Connor et al., 2005; Markowicz et al., 2008). Its temporal resolution was around 15 s for this deployment, which is slightly coarser than the WACR's. Here, it is assumed that each reported base height is representative of the whole 15 s. The ceilometer range resolution is 15 m. Thus, the analysis is done using the original WACR temporal grid, thus, maintaining the high sampling rate of the WACR. The ceilometer was deployed for the whole duration of the campaign. It only experienced 12 downtimes lasting more than an hour (including three covering more than a day), as well as a small number of shorter interruptions (see the dark bars in Fig. 1).

2.3 Microwave radiometer

A standard "mailbox" microwave radiometer (MWR) was also present throughout the campaign. This instrument passively measures the amount of radiation emitted by the atmosphere at two frequencies (23.8 and 31.4 GHz) to retrieve the amount of integrated water in the atmospheric column above, separated into the vapor and liquid phases (respectively the precipitable water vapor (PWV) and liquid water path (LWP); e.g., Liljegren, 1994). Such information can help to constrain retrievals from other instruments, such as the WACR. The MWR time resolution is around 30 s, which is also coarser than the WACR's. Nevertheless, as the MWR measurements actually come from 20-s signal dwells, it is reasonable to consider each retrieved quantity to be representative of the whole 30 s. Therefore, these measurements are oversampled to match the high temporal resolution of the WACR when required by the analysis. As with the ceilometer, the MWR was deployed for the whole campaign, and it worked continuously without much interruption of data (see Fig. 1, light bars). However, the MWR experienced a processing problem in the second summer, rendering the measurements reported from June 11 through August 9, 2010 unreliable (not shown in Fig. 1 as measurements are available nevertheless).

2.4 Radiosondes

Regular radiosonde launches (every six hours) were performed throughout the deployment to characterize the thermodynamic state of the atmosphere, as well as the wind speed and direction. The radiosondes collect measurements every 2 s during its ascent, providing a typical vertical resolution of 10 m in the troposphere (depending on the conditions at the launch time). These measurements can only be interpolated to the WACR time steps with limited confidence, due to the coarse temporal resolution of the radiosondes. However, some statistics can still be determined around the balloon launch times, since there are 20 months of data, comprising more than 2200 atmospheric

profiles, although no sondes were launched in the last third of October 2009, nor from December 2, 2009 through January 12, 2010 (see the numbers on top of Fig. 1).

3. METHODOLOGY

The sensors described above have certain capacity for detecting the presence of clouds in the overlaying atmospheric column. For instance, relative humidity profiles taken by a radiosonde have been used in the past to provide estimates of cloud layer locations (e.g., Wang and Rossow, 1995). But, their temporal resolution is too coarse to form robust statistics of cloud occurrence especially in the MBL, where clouds are typically very thin. The MWR is sensitive to the presence of liquid in the column, and measurements above its theoretical sensitivity (30-50 gm^{-2}) can be used to infer the occurrence of liquid clouds. However, the MWR misses all ice clouds (mostly cirrus clouds in the Azores), as their emissions are negligible at the frequencies sensed by the MWR (Ulaby et al., 1981). Similarly, the ceilometer measurements are very sensitive to the presence of cloud droplets, providing a good estimate of the base height of liquid clouds; its backscatter profiles can be used to find ice cloud too (e.g., Liu et al., 2009). Nevertheless, it still misses most high clouds, as its useful range stops near 7.5 km. Finally, the WACR is sensitive to most hydrometeors, and profiles all clouds in the troposphere, unless strong precipitation occurs and causes too much attenuation (Lhermitte, 1990). However, it cannot easily differentiate precipitation from cloud particles (so cannot be used to reliably provide cloud base estimates in drizzling conditions), and lacks sensitivity to very thin liquid clouds (less than 100 m thick).

Here, a multi-instrument approach that utilizes synergetic measurements from all sensors is used to describe the cloud and precipitation conditions during CAP-MBL. Due to the focus on describing the vertical structure of clouds and precipitation, only the active remote sensors (radar/lidar) measurements are used for the cloud and precipitation occurrence statistics, while the MWR and the soundings are used as additional classification variables. The approach is not new, the cloud radar and lidar are

complementary instruments often used to derive cloud and precipitation statistics (e.g., Intrieri et al., 2002; Bretherton et al., 2004; Kollias et al., 2007b, Illingworth et al., 2007).

Using the raw WACR measurements (radar reflectivity and Signal-to-Noise Ratio (SNR)), the radar range gates that contain significant returns from atmospheric targets (e.g., hydrometeors) are identified to develop the radar-detected hydrometeor mask. The large number of WACR integrated radar pulses (~20,000 collected in 2 sec signal dwell and a WACR Pulse Repetition Frequency of 10 kHz) enables to detect very low signal to noise radar returns in the boundary layer (WACR sensitivity of -56 dBZ at 1 km). The significant detection WACR hydrometeor mask is based on Clothiaux et al., 1995, and a two-dimensional (time-height) filter is used to remove isolated radar pixels. The WACR-derived hydrometeor mask is used to estimate the number of hydrometeor layers in the atmospheric column and their corresponding boundaries. The WACR-derived hydrometeor layer base is not necessarily the cloud base since the WACR cannot differentiate between cloud and precipitation particles below the cloud base. Thus, the radar-derived hydrometeor mask is combined with the ceilometer-generated time series of cloud base heights. Although the ceilometer detects drizzle too, its measurements are more sensitive to the numerous small liquid cloud droplets encountered by the laser at the cloud base, and thus are systematically used to derive the liquid cloud base, at least for the first cloud layer. As formerly observed (e.g., Comstock et al., 2004; Wood et al., 2011), heavy drizzle often give false signals, by significantly lowering the derived cloud base height. Given the likely situation for heavy precipitation to form, the cloud identification will still be reliable. However, further analysis of MBL clouds would be affected. Thus, the profiles containing intense precipitation (defined below) are removed prior to subsequent analysis.

The WACR/ceilometer detections agree very well in the MBL, however, the possibility of underestimating the hydrometeor occurrence at high altitude should be considered since the ceilometer is not capable of detecting high clouds and the radar sensitivity is degraded. The WACR moments, the radar-derived hydrometeor mask and the ceilometer-derived liquid cloud base are input in the cloud and precipitation type identification scheme described in the following section.

3.1 Cloud and precipitation type identification

Here, precipitation requires the detection of hydrometeors by the WACR below the ceilometer cloud base. Three precipitation types are identified according to their minimum detection height and intensity at the surface (here taken as the lowest radar gate, around 170 m AGL; see Table 1a). Virga is here defined as precipitation that does not reach the lowest WACR range gate (i.e. no significant radar return at its lowest range gate). Precipitation that reaches the WACR lowest range gate is classified as light and intense using a near-surface (200 m) radar reflectivity threshold of 0 dBZ. Moreover, anytime the WACR lowest gate echoes have a reflectivity above 0 dBZ, intense precipitation is identified, relaxing the requirement mentioned above since the ceilometer measurements are significantly affected by the presence of water on its lens cover.

Using the WACR-derived hydrometeor mask and the ceilometer-derived cloud bases, hydrometeor clusters are identified. Each cluster is individually analyzed on an hourly basis, with the hydrometeor layer base (top) defined as the 5^{th} (95^{th}) percentiles of the hourly distribution of the cloud cluster base (top). Based on their hourly-derived base and top height extrema and the available ceilometer-derived cloud base height, several cloud types are identified (Table 1b). The hourly clusters are first separated into 4 types based specifically on these boundary definitions: 1) high cloud if the base is above 7 km; 2) middle cloud if the base is above 3 km; 3) low cloud if the top is below 3 km; and 4) deep BL cloud if the base is below 3 km, but the top is above 3 km. Note that the last category contains mostly frontal clouds, such as nimbostratus and cumulonimbus. Since the focus of this study is MBL clouds, emphasis is placed on low clouds, where the radar and lidar are most sensitive, allowing for well defined cloud boundaries. As a result, low clouds are further divided into three sub-types. The horizontal (temporal) duration of a hydrometeor cluster is used to differentiate broken cloud conditions (shallow cumulus) from stratiform cloud conditions, while stratocumulus are also required to have a narrow hourly cloud top height distribution (less than 100 m standard deviation). Examples of stratiform and broken MBL cloud conditions as seen by the WACR and MODIS are

shown in Fig. 2. The remaining low cloud hourly clusters make up the third sub-type (referred to as indeterminate hereafter). Each cloud type has an expected precipitation type (last row of Table 1b), although others are also possible. Note that the lidar measurements rarely reach high clouds, and thus no precipitation shaft is expected. Note also that the cloud types are not all mutually exclusive, since only two dimensions are observed and clouds are evolving.

The cloud and precipitation identification scheme is applied each day that both the WACR and ceilometer were operational, and statistics about cloud and precipitation occurrences are computed on hourly and daily basis, with the daily results composited together to form monthly statistics. Note that the hourly-derived boundaries extrema are only used to identify the cloud types. Further analysis makes use of the full hourly distribution of the cloud base and top heights to provide their statistics. Finally, the occurrences of cumulus clouds under a stratocumulus cover are investigated. These represent the WMO-defined low cloud type CL8, and are diagnosed on an hourly basis. When both types are detected in any number of profiles within an hour, all profiles having cumulus and/or stratocumulus clouds within that same hour are included in the Sc+Cu category.

3.2 Radiosonde analysis

Radiosonde data are not used directly in cloud identification, but are used to determine the thermodynamic structure of the lower atmosphere during certain cloud conditions. For instance, the inversion often associated with the top of the MBL is easily detected in sounding profiles. A temperature increase with height somewhere between 500 m (to avoid surface effects) and 3 km (to remain in the MBL) denotes the presence of an inversion. The level of maximum increase indicates the inversion layer location, and it includes all levels around it still characterized by an increase. Since wetting affects the temperature measurements above clouds (Caldwell et al., 2005), a loose criterion on the water vapor mixing ratio (r) was added by requiring its decrease with height.

Many studies have also mentioned the presence of a transition layer in the MBL, which separates a surface mixed layer from the cloud containing layer aloft (Augstein et al., 1974; Garstang and Betts, 1974; Yin and Albrecht, 2000). It is mainly characterized by a sharp decrease of moisture with height, accompanied by a slight increase in temperature. It indicates the presence of decoupling conditions that can lead to a cut-off of the upper part of the MBL from its moisture supply, thus controlling low-level cloudiness. Cumulus clouds often form near its top, as the lifting condensation level often falls within the transition layer (Yin and Albrecht, 2000). Following Yin and Albrecht (2000), the presence of a transition layer will be investigated using their parameter μ, which combines the potential temperature θ and mixing ratio r gradients. Its mean value is computed using all levels below the inversion. Then, if the maximum value of μ in those levels is positive and greater than 1.3 times the mean (based on Yin and Albrecht, 2000), a transition layer is present. The transition layer includes all levels around the μ maximum that satisfy this criterion.

As the detection of these two layers depends on the derivative of the measured variables, a 1-2-1 smoother is applied prior to any analysis. This step removes most of the small-scale variability that might be caused by sampling errors, and provides smooth local gradients. Also, when averaging various profiles together, a layer-by-layer procedure is used to preserve the character of the transition and inversion layers (based on Augstein et al. (1974) and Yin and Albrecht (2000)).

The lower tropospheric stability (LTS) is also used in this study. Based on Klein and Hartmann (1993), it is defined as the difference in potential temperature between 700 mb and the surface. Finally, any interpolated (or averaged) wind direction is obtained from the two interpolated (or averaged) components of the wind vector.

3.3 Turbulence and mass flux measurements

During non-precipitating cloud conditions, the WACR Doppler velocity measurements are used to derive turbulence statistics in low-level stratiform cloud conditions. This is

based on the assumption that liquid cloud particles have negligible terminal velocity and inertia, and thus act as tracers of the vertical air motion (e.g., Kollias et al., 2001). Only stratocumulus periods without drizzle detected under the ceilometer base are considered in these statistics, in order to remove most bias caused by the larger precipitating particles. The WACR Doppler velocity measurements are used to estimate the hourly estimates of the mean, variance and skewness of the vertical air motion. Using the vertical air motion measurements, mass flux statistics are also estimated during non-precipitating stratocumulus conditions to reduce any correlations between drop fall velocities and WACR Doppler measurements. Using the high-resolution in-cloud vertical velocity measurements the mass flux profiles are derived using direct and conditional sampling (based on Kollias and Albrecht, 2000).

The direct sampling method is applied using the WACR perturbation velocities.. These are obtained by removing the hourly mean from the velocity measurements. The direct method can be refined to retrieve the contribution from the cloud's coherent structures only. Those structures are pockets of cloud that move together on average. The coherency must be observed in both dimensions: the perturbed vertical velocity must conserve its sign for three or more successive profiles (time dimension, which relates to the horizontal dimension), and over at least four successive gates (i.e., about 170 m in the vertical dimension).

The mass flux profiles are also computed using the turbulence statistics as proposed by Randall et al., 1992. This method relates the fractional updraft area and the mass flux to turbulence statistics. It uses a "top hat" representation of the updrafts and downdrafts properties to express the fractional updraft area and updraft and downdraft velocities as functions of the vertical velocity first three moments (mean, variance, and skewness). A mass flux relationship is then obtained, and it depends only on the variance and skewness of the vertical velocity (see Randall et al. (1992) for the actual equations, and their complete derivation).

4. RESULTS

4.1 Cloud and liquid precipitation occurrence

Using the radar/lidar synergetic observations, the monthly fraction of time hydrometeors were detected in the atmospheric column is shown in Fig. 3a. A weak seasonal cycle is observed with minimum (60–70%) during the summer and early fall and maximum (80%) during the winter and spring season. Liquid precipitation is detected almost 50% of the time we have hydrometeors in the atmospheric column and exhibits a similar weak seasonal cycle. A breakdown of the observed cloud occurrence into the four main cloud types (described in section 3.1) is shown in Fig. 3b. Note that the sum of these cloud type occurrences is likely greater than (rather than equal to) the overall cloud occurrences shown in Fig. 3a, since more than one cloud type can be present in the atmospheric column at the same time. Low-level clouds are the dominant observed cloud type, with 40–60% occurrence maximizing in the summer and fall seasons. The seasonal cycle of low cloud occurrence anti-correlates with the observed seasonal cycle of all the other cloud types which peaks during the winter and spring seasons (Fig. 3b), consistent with the presence of the subtropical high-pressure system during the summer and fall seasons that favors MBL cloud occurrence through the development of low tropospheric stability and moisture trapping in the low levels. This system is strongest in summertime, when midlatitude storm tracks are at their most poleward, and with its center closer to the site (Hasanean, 2004), explaining the trends observed, as proposed by Norris and Klein (2000).

Additional insights on the seasonal cycle of low-level clouds are provided through their breakdown into different subtypes (see Fig. 3c). Shallow cumulus clouds are the most frequently observed MBL cloud type with a monthly occurrence of 20% and weak variability during the summer. The intraseasonal variability is likely linked to the decoupling of the MBL, as it coincides with increases in the Sc+Cu coverage. Indeed, this MBL cloud structure is also frequently observed, with maximum occurrences during the summer months. In fact, they follow a similar annual cycle as the single-layer

stratocumulus clouds, which are the least observed MBL cloud type especially during winter and spring months. Nevertheless, the dataset is not long enough to derive robust seasonal climatology, as evinced by the differences between months in the first and second years. As for the indeterminate category, it has typical occurrences around 10% with small intraseasonal variability. Such low values probably come from the intermediate state of this type, acting as a transition between the other clouds based in the MBL (i.e., low and deep BL clouds).

The LTS has often been linked to the presence of low clouds. For instance, Zhang et al. (2010) provided coarse threshold values of LTS for small and high low-cloud fractions, respectively less than 14K and greater than 19K. These values correlate well with the cumulus and stratocumulus covers (see Fig. 3e). In fact, increases in LTS are usually associated with increases in stratocumulus coverage. Moreover, most values are close to, or above, the 14K threshold, allowing cumulus clouds to form. This emphasizes the greater stability (mean of 17K) found in the Azores, compared to the eastern equatorial Pacific (13K, see Yin and Albrecht, 2000).

Fig. 3a demonstrates the propensity of marine clouds to produce precipitation. However, it often completely evaporates before reaching the surface, as illustrated by the separation into the three types considered (virga, light, and intense) in Fig. 3d. Intense precipitation occurs mostly during fall and winter, weakly following the presence of deep BL clouds, demonstrating that it is primarily associated with stronger and deeper systems. Other precipitation categories display no obvious annual variability.

4.2 Stratocumulus and cumulus cloud base height statistics

According to Table 1b, stratocumulus and cumulus clouds are separated based on their horizontal extent. Furthermore, their cloud base height statistics are different and this improves the robustness of the radar-lidar based classification algorithm. The distributions of their hourly-averaged cloud base heights are compared in Fig. 4a. Only hourly periods with a cloud fraction greater than 10% for the given type are included in

the analysis. Furthermore, any hourly period with intense precipitation is also excluded to avoid possible contamination of the ceilometer cloud base. Although considerable variability in the cloud base occurrences of these two cloud types is observed, a separation is clearly visible between the two distributions, with cumulus clouds forming lower than stratocumulus clouds. This is consistent with the frequently observed cumulus under stratocumulus MBL cloud structure in Azores. Yet, some stratocumulus bases have been detected at very low altitudes (below 500 m, below most cumulus). Such low-based stratocumulus clouds have been sampled during ASTEX (de Roode and Duynkerke, 1997). The hourly-averaged stratocumulus cloud top height and cumulus cloud base height correspond well with the MBL inversion base and the transition layer top respectively (Fig. 4b). The MBL inversion base and transition layer top are estimated from the radiosondes, while the cloud boundary heights are averaged over the hour containing the sounding launch time. As before, 10% coverage is required, without intense precipitation. The results are again in nice agreement with the expectations: both distributions are peaking near a zero difference, although the cumulus cloud base exhibits higher variability around the transition layer top. This greater variability for cumulus clouds might be caused by the difficulty of correctly detecting the transition layer and from cumulus clouds linked to other clouds (i.e., breaking deep BL, stratocumulus or indeterminate clouds).

The double-peak cloud base height structure observed for the stratocumulus clouds is explained by their seasonal cycle (Fig. 5a). The lower peak (around 1100 m) results from summer cases, while the higher peak (around 1600 m) results from the transition periods (spring and fall, mainly May and September). The winter season did not experience much stratocumulus coverage (as noticed in Fig. 3c), and thus does not contribute much. The agreement between the stratocumulus tops and the inversion base is still visible after averaging them monthly, except in winter when the stratocumulus clouds are less frequent (Fig. 5a). Another noticeable finding is the very frequent occurrence (higher than 80%) of inversion and transition layers in the MBL through out the field campaign (Fig. 5b). The occurrence is based on the monthly fraction of soundings with inversion and/or transition layers. The persistence of transition layers indicates the luck on well-mixed conditions in the subcloud layer.

4.2.1 MBL variability during single and multilayer cloud conditions

A detailed analysis of the MBL variability during stratocumulus and stratocumulus over cumulus conditions and their corresponding MBL thermodynamic structure is presented here. Every hour of the day, the fraction of time multilayer cloud conditions is recorded along with the average difference between the cloud base heights of the two layers. If multilayer conditions exist for more than 10% of the hour and the cloud base height difference is larger than 300 m, then the hour is classified as a multilayer cloud condition. On the other hand, if a single cloud layer is only detected within the hour and the cloud base variance is less than 100 m, then the hour is classified as single layer cloud conditions. Using the number of hours every month classified as single or multilayer cloud conditions, their diurnal and seasonal cycle can be estimated (Fig. 6). The observations suggest the presence of a weak diurnal cycle with increased single-layer occurrences during daytime, and the opposite for the multilayer conditions. Although this seems counter-intuitive from a decoupling view, it is supported by the near-constant decoupled state of the MBL (see Fig. 6b), allowing cumulus to be omnipresent, while stratocumulus tends to fill in preferably during nighttime. On the other hand, the MBL does show more multi-layer cases in the wintertime and more single-layer clouds in the summertime, with associated inverse trends in the spring and fall seasons. This result is consistent with a weaker high-pressure system in winter, allowing for a weaker, and higher (see Fig. 5a), inversion, providing more vertical extend to form multiple clouds.

The sounding collected within an hour of single and multilayer cloud conditions are further analyzed to identify the main feature of their corresponding thermodynamic structure in the MBL. Each sounding is first separately analyzed to detect the height of the inversion and transition layers (if present). The analysis indicated that the vast majority of the analyzed soundings that correspond to both single and multilayer cloud conditions show a transition layer (Fig. 5b). The soundings that did not have a detectable transition layer in the MBL were shallow (inversion height below 1 km), which might have prevented the complete formation of a transition layer. This concurs with previous

studies (Albrecht et al., 1995; Wood and Bretherton, 2004) suggesting that the atmospheric BL must be deeper than about 700 m to have a decoupled structure.

The single cloud (stratocumulus and cumulus) layer soundings are separated in two subsets, according to the thermodynamic layer linked to the cloud layer: inversion (stratocumulus) and transition (shallow cumulus). A third category of soundings corresponds to multi-layer cloud conditions (stratocumulus with cumulus underneath). Using all the soundings with a transition layer, composited profiles were obtained for each group following the layer-by-layer averaging method described in section 3.2 (see Fig. 7). The cases of single layer at the inversion (stratocumulus) have a lower average inversion height, reminiscent of the difficulty to fully decouple shallow MBL. They also have the strongest potential temperature and mixing ratio jumps through the inversion layer associated with the weakest jumps at the transition layer, supporting only the stratocumulus cloud. Comparatively, both layers show strong jumps for the cases of single cloud layer at the transition (cumulus). A strong inversion in both types of single layer cases is consistent with their tendency to occur during summer, when the high-pressure system is stronger. The averaged profiles of potential temperature and mixing ratio exhibit a gradual transition from the stratocumulus to stratocumulus-with-cumulus and cumulus-only cloud regimes. The profiles with the lowest relative humidity correspond to cloud conditions associated with the transition layer only (cumulus). Multi-layer cloud conditions are associated with high wind magnitude. The wind direction averaged profiles are very similar above the base of the transition layer; however, an easterly wind at the surface seems to be linked with single cloud layer detections near the inversion. These last results need further analysis to physically explain them properly.

The MBL thermodynamic structure during low cloud conditions was further investigated using the sounding directly without classifying them by cloud type (see Fig. 5b). Inversion-topped MBL were encountered for all the soundings except a few representing less than 5% of the soundings, although those non-topped MBL occur mostly in wintertime. Similarly, most soundings presented a transition layer signature (92%), but without preference on the timing. This is consistent with the constant detection of cumulus clouds.

The proportions of transition and inversion layers found in soundings are much larger than observed over the eastern equatorial Pacific (Yin and Albrecht, 2000), accounting for a different environment. It is reasonable to hypothesize that, to support a well-defined transition layer, significantly strong mixing in the upper layer is required to support a clear temperature jump at its base. Radiative cooling associated with extensive clouds in the upper MBL may provide such mixing. In purely trade cumulus BL, this mixing is less efficient and the transition layer is less well defined. Interestingly, the transition layer height closely follows the inversion base height on a monthly basis (see Fig. 5a), which further supports this hypothesis.

4.3 Stratocumulus clouds

4.3.1. Macroscopic properties and thermodynamic structure

Using the hours with single layer stratocumulus conditions, thirty-five days where stratocumulus clouds persist through most of the day are selected for additional analysis. The days are listed in Table 2, along with some daily-averaged macroscopic properties of the cloud layer and thermodynamic structure. Most of the selected days occurred in early summer (June–July) or late fall (October–November). During the summer period, stratocumulus clouds have lower cloud base heights compared to the late fall (bimodal structure Fig. 8a). Distinct difference in the distribution of cloud thickness is observed during drizzling (excluding intense precipitation) and non-drizzling conditions. The distribution of cloud thicknesses for periods with a drizzle shaft peaks around 250–300 m, while, the distribution of cloud thicknesses for periods without virga peaks at 150 m (Fig. 8b). On the contrary, there is no clear difference in the distributions of cloud bases using the same separation (see Fig. 9a). The peak below 200 m for the cases "without drizzle" comes mostly from periods when the ceilometer measurements are compromised by heavy precipitation, as they correspond to the tail of larger depths seen in Fig. 8b.

Another way to demonstrate the difference in cloud thickness during drizzling and non-drizzling periods is through their corresponding distributions of LWP (see Fig. 8c). Although small amounts are possible in all stratocumulus clouds, LWP greater than 75–100 g/m^2 are sufficient to produce drizzling conditions. This result compares well with previous studies conducted in various stratocumulus decks (e.g., Wood, 2005; Zuidema et al., 2005; Serpetzoglou et al., 2008; Kubar et al., 2009). Moreover, the non-drizzling distribution peaks around 30 g/m^2, which is near the theoretical accuracy of the deployed MWR. Also, as before, the low tail of greater LWP visible for the non-drizzling profiles is associated with the deep and low clouds affected by precipitation.

The soundings recorded during the selected thirty-five days are used to describe the inversion and transition layer characteristics. As expected, all the recorded soundings indicate the presence of an inversion layer near the stratocumulus cloud top. Due to their small number (141) and the difficulty to properly define the associated drizzling character, no separation was performed. The depth of the inversion layer shows a strong peak just below 200 m (see Fig. 8d), although wetting might have inflated this derived quantity, mainly through an overestimate of the layer top (see Caldwell et al., 1995). The daily-averaged strength of the inversion layer in terms of potential temperature ($\Delta\theta$) and water vapor mixing ratio (Δr) is included in Table 2, while the full distributions of the jumps in equivalent potential temperature ($\Delta\theta_e$) and r are given in Fig. 7e. As observed in various stratocumulus studies, $\Delta\theta_e$ is often negative. Nevertheless, this situation can still satisfy the stability criterion (Kuo and Schubert, 1988), since Δr is usually also negative, depending on the processes considered in the criterion. Based on the methodology devised by Yin and Albrecht (2000) for the East Pacific (as described in section 3.2), the presence of a transition layer was also diagnosed for most of the persisting stratocumulus soundings, as the threshold value was usually exceeded (see Fig. 8f).

4.3.2 Diurnal cycle

Using the hourly-derived statistics from the thirty-five selected days, a composite daily cycle is derived for the occurrence and boundaries of the stratocumulus clouds and their

associated drizzle, using 3-hour bins (Fig. 9). As expected, the cloud fraction is very high (>80%) throughout the day. The maximum values of cloud fraction are found during nighttime, with a gradual decrease of coverage occurring in the morning hours, followed by an increase after sunset. The marine stratocumulus clouds observed at Azores are usually precipitating (70% of the time), and the small decrease in cloud fractional coverage during daytime is also associated with a reduced drizzling fraction reaching ground. In fact, while virga is constantly detected in 45% of an average stratocumulus, shallow precipitation has a marked decreased occurrence during the day. As for intense precipitation, it rarely occurs in a stratocumulus (less than 5%), and it is mostly around sunset and sunrise. Note that the following panels of Fig. 9 show pseudo-daily cycles, as they mix periods from various cases.

Shallow MBL are needed during nighttime to observe non-dizzling conditions, as indicated by the lower cloud boundaries, while the development of drizzle during daytime does not depend on the MBL depth (Fig. 9b). Shallow drizzle periods correspond to thicker cloud decks (450–550 m compare to 200–270 m) and higher LWP values (140–200 gm^{-2} to 30–60 gm^{-2}). Interestingly, virga periods have similar cloud depths (around 300 m) as the non-drizzling periods, but constantly show larger LWP values (70–100 gm^{-2}). Furthermore, only the LWP of virga periods have a distinctive daily cycle, with a pronounced increase near sunset. A similar cycle is observed in the cloud depth of the shallow drizzle periods, following its stratocumulus coverage (Fig. 9c-d).

4.3.3 Air mass origin

The origin of the atmospheric air mass associated with the selected days is investigated using the HYSPLIT backward trajectories (see the last column in Table 2). The trajectories were traced back over a week, at three heights in the BL. For each case, an ensemble of trajectories was also performed, covering 5 days, to ensure the robustness of the results. Finally, the consistency of the origin was revised looking at trajectories obtained at two hours interval during an event. It appears that the most persistent cases of spring and summer have maritime origins (trajectory over the ocean throughout the

previous week), while those in fall seem to have a more continental origin (trajectory over a continent during the first few days at least). This could account for other macrophysical differences, such as the height variability. It is also quite probably linked to the strength of the high-pressure system. However, a more detailed analysis is needed to draw conclusions.

4.3.4 Vertical air motion statistics

Vertical air motions play an important role in the evolution of stratocumulus. Considering only the time periods without a drizzle shaft in the 35 selected cases, hourly vertical air motion statistics are derived (section 3.3). Hours with less than 15% non-drizzling coverage are discarded from the following analysis. In the analysis, positive velocities indicate updrafts. Thus, negative skewness of the hourly distribution of vertical air motion indicates the presence of a few strong narrow downdrafts compensated by many weak broader updrafts. Daytime and nighttime composites of the vertical air motion statistics are constructed to highlight differences between day (11:00–17:00 UTC) and night (23:00–05:00 UTC) time periods. Time periods close to local sunrise or sunset are discarded from this type of analysis to ensure a clear separation between the two periods.

The vertical air motion variance profiles peaks at the cloud base (Fig. 10a). As noted in previous studies of the MBL (e.g., Nicholls, 1989; Hignett, 1991), it indicates a maximum of turbulent kinetic energy near the middle of the MBL since our measurements cover the top part of the MBL occupied with cloud. Higher variance is observed during nighttime, as observed by Hignett (1991), consistent with cloud top-driven turbulence due to cloud-top radiative cooling. This excess turbulent energy is responsible for the thickening of the stratocumulus deck, its higher cloud fraction and stronger drizzle presence. The nighttime skewness profile of the vertical air motion is negative throughout the cloud layer (Fig. 10b). This is consistent with cloud-top radiative cooling as the driving mechanism and most nocturnal in situ observations (e.g., Kollias

and Albrecht, 2000). During daytime however, skewness values are closer to neutral in the lower two thirds. Near the cloud top, both periods show a similar behavior again, decreasing to strong negative values, suggesting cloud-top driven turbulence.

The diurnal evolution of the vertical air motion variance and skewness in the stratocumulus layer is shown in Fig. 9c,d using 3-hour bins. The vertical air motion variance maximum is still clearly depicted at night in the bottom half of the cloud. The periods exhibit the highest variance values in the lower part of the cloud: 21:00–24:00 UTC and 03:00–09:00 UTC. Minimum vertical air motion variance in the lower part of the cloud is observed during the 12:00–18:00 UTC period. Close to the cloud top, the variance appears consistently low through the day. The diurnal cycle of the vertical air motion skewness better captures the role of cloud-top radiative cooling as a source of turbulence during nighttime. Positive values are also observed, but mostly in the top half during daytime, especially around noon when positive values appear to take over the whole cloud, consistent with surface-driven turbulence.

4.3.5 Updraft mass flux

The in-cloud vertical air motions support a significant portion of the turbulent transport of heat and moisture in the cloud layer. The turbulence transport is often organized in temporally-spatially coherent updraft and downdraft structure. Here, the vertical air motion measurements are separated into nighttime and daytime periods and the analysis described in section 3.3 is applied to estimate the mean updraft and mean downdraft velocity profiles, the updraft area profile and the updraft mass flux profile. The resulting in-cloud profiles are shown in Fig. 11, using the three possible methods (direct, coherent and statistical). First, note that the statistical technique gives generally the same profiles as the direct sampling, despite a small overestimate of the magnitudes, as found in LES models (Randall et al., 1992) and continental stratocumulus (Kollias and Albrecht, 2000).

The mean amplitudes of velocity in updrafts and downdrafts are very similar. This is linked to the cloud separating into two halves (one going up, the other going down) on

average throughout its depth, which compares well with continental stratocumulus clouds (e.g., Kollias and Albrecht, 2000), and other marine cases (e.g., Nicholls, 1989; de Laat and Duynkerke, 1998). However, coherent structures are responsible only for 40–60% of the total mass flux. The contribution of coherent structures to the turbulent transport is maximized at night near the middle of the cloud. The mean velocity of coherent structures is also stronger, as expected. Nevertheless, their contribution to the mass flux is still limited, especially during daytime. As observed in the majority of stratocumulus decks, the mass flux is greater during nighttime, and in the bottom half of the cloud, when and where the turbulence is stronger. It is also linked to the mean velocities being maximized near the cloud base (~0.5 m/s), decreasing with height.

A similar analysis performed at the cloud base of cumulus return comparable values, although the night and day results are closer. The main differences are stronger mean updraft and downdraft velocities, and a weaker contribution from nighttime coherent structures.

5. SUMMARY

The CAP-MBL campaign led to the collection of an extensive and well documented, ground-based dataset of MBL clouds. Here, emphasis is given to the development of a comprehensive description of the cloud and precipitation conditions during the field campaign. Several remote sensors are used to develop statistics of occurrence of various cloud and precipitation types. Clouds occur frequently throughout the 19-month period that was analyzed (June 2009–December 2010), with a maximum (80%) during the winter-spring months and a minimum (60–65%) during the summer months. Precipitation occurrence is also very high (30–40%), but precipitation only reaches the ground less than 15% of the time it is precipitating. Most intense precipitation events correlate well with the occurrence of non-MBL clouds linking them to mid-latitude cyclones during the winter and spring months.

A predominance of MBL clouds was observed all year long, while higher clouds show enhanced occurrences in winter. Moreover, cumulus clouds are present during all seasons, while stratocumulus clouds occur preferably during the transition periods. These two types often occur together, with each type being tied to a distinct thermodynamic layer (the cumulus to the transition layer, and the stratocumulus to the inversion layer). The strength of the subtropical high-pressure system influences the height (and presence) of the inversion, thus regulating the height of the stratocumulus layer, as well as the possibility to create two cloud layers in the MBL. In fact, on average, a stronger θ increase, a greater LTS value, and a lower inversion base tend to accompany a greater surface pressure at Azores (a proxy for the strength of the subtropical anticyclone). In turn, a higher pressure also seems more favorable for a stratocumulus formation alone, while the cumulus clouds would form underneath at lower surface pressure.

Analysis of the sounding profiles demonstrates the near omnipresence of decoupling in the Azores MBL, a new finding that is only made possible by the long measurements made during the campaign. Cloud layers do not always reveal this decoupling, presenting only one layer in the observations. Two explanations can be hypothesized. First, a strong transition layer could prevent moisture from reaching the upper cloud layer. Second, a transition layer too weak might be unable to efficiently prevent the vertical development of cumulus clouds that would then fusion with the stratocumulus layer. Stronger winds are associated with the presence of clouds in both layers, although a more detailed investigation is needed to verify this.

Thirty-five days characterized by the presence of persistent single-layer stratocumulus clouds were selected to gain further insights on their diurnal cycle, their macroscopic properties (LWP, cloud boundaries) and dynamics. The minimum coverage is observed in the afternoon. This is consistent with other studies findings using ground-based and satellite observations and models (e.g., Rozendaal et al., 1995; Abel et al., 2010). Although the fractions found here are greater (remaining above 80%), this is probably a bias due to the selection of persisting stratocumulus layers. Diurnal clearing is accompanied by a thinning of the cloud layer, and a decrease in ground precipitation coverage and LWP. Again, this is consistent with other stratocumulus studies, such as those performed in the South-East Pacific (e.g., Wood et al., 2002; Abel et al., 2010).

Furthermore, it was observed that stratocumulus is most likely to drizzle if the cloud depth exceeds 250 m and the LWP is above 60 g/m^2. Local maxima of ground precipitation coverage occur around sunrise and sunset.

We find that stratocumulus clouds are more turbulent during nighttime. Throughout the day, the turbulence maximized in the bottom half of the cloud, except around sunrise and after sunset when it extended through higher levels. Profiles of skewness from the velocity time series are consistent with cloud-top radiative cooling during nighttime, and surface heating around noon, as reported in many other stratocumulus clouds (e.g., Kollias and Albrecht, 2000). Mass flux is greater at night, with the updrafts covering about half of the cloud, in accordance with observations in other decks and current theories (e.g., Nicholls, 1989; de Laat and Duynkerke, 1998; Kollias and Albrecht, 2000). However, the contribution from coherent structures is more limited than observed in continental stratocumulus clouds.

6. REFERENCES

Abel, S. J., D. N. Walters, and G. Allen, 2010: Evaluation of stratocumulus cloud prediction in the Met Office forecast model during VOCALS-REx. *Atmos. Chem. Phys.*, **10**, 10541–10559, doi:10.5194/acp-10-10541-2010.

Albrecht, B. A., C. S. Bretherton, D. W. Johnson, W. H. Schubert, and A. S. Frisch, 1995: The Atlantic Stratocumulus Transition Experiment—ASTEX. *Bull. Amer. Meteor. Soc*., **76**, 889–904.

Augstein, E., H. Schmidt, and F. Ostapoff, 1974: The vertical structure of the atmospheric planetary boundary layer in undisturbed trade winds over the Atlantic Ocean. *Bound.-Layer Meteor.*, **6**, 129–150.

Bony, S., and J.-L. Dufresne, 2005: Marine boundary layer clouds at the heart of tropical cloud feedback uncertainties in climate models. *Geophys. Res. Lett.*, **32**, L20806, doi:10.1029/2005GL023851.

Bretherton, C. S., T. Uttal, C. W. Fairall, S. Yuter, R. Weller, D. Baumgardner, K. Comstock, R. Wood, and G. Raga, 2004: The EPIC 2001 stratocumulus study. *Bull. Amer. Meteor. Soc.*, **85**, 967–977.

Caldwell, P., C. S. Bretherton, and R. Wood, 2005: Mixed-layer budget analysis of the diurnal cycle of entrainment in Southeast Pacific stratocumulus. *J. Atmos. Sci.*, **62**, 3775–3791.

Clothiaux, E. E., M. A. Miller, B. A. Albrecht, T. P. Ackerman, J. Verlinde, D. M. Babb, R. M. Peters, and W. J. Syrett, 1995: An evaluation of a 94-GHz radar for remote sensing of cloud properties. *J. Atmos. and Oceanic Technol.*, **12**, 201–229.

Comstock, K. K., R. Wood, S. E. Yuter, and C. S. Bretherton, 2004: Reflectivity and rain

rate in and below drizzling stratocumulus. *Q. J. R. Meteorol. Soc.*, **130**, 2891–2918.

de Laat, A. T. J., and P. Duynkerke, 1998: Analysis of ASTEX-stratocumulus observational data using a mass-flux approach. *Bound.-Layer Meteor.*, **86**, 63–87.

de Roode, S. R., and P. G. Duynkerke, 1997: Observed Lagrangian transition of stratocumulus into cumulus during ASTEX: Mean state and turbulence structure. *J. Atmos. Sci.*, **54**, 2157–2173.

Garstang, M., and A. K. Betts, 1974: A review of the tropical boundary layer and cumulus convection: Structure, parameterization and modeling. *Bull. Amer. Meteor. Soc.*, **55**, 1195–1205.

Harrison, E. F., P. Minnis, B. R. Barkstrom, V. Ramanathan, R. D. Cess, and G. G. Gibson, 1990: Seasonal variation of cloud radiative forcing derived from the Earth Radiation Budget Experiment. *J. Geophys. Res.*, **95**, 18687–18703.

Hasanean, H. M., 2004: Variability of the North Atlantic subtropical high and associations with tropical sea-surface temperature. *Int. J. Climatol.*, **24**, 945–957.

Hignett, P., 1991: Observations of diurnal variation in a cloud-capped marine boundary layer. *J. Atmos. Sci.*, **48**, 1474–1482.

Illingworth, A. J., R. J. Hogan, E. J. O'Connor, D. Bouniol, M. E. Brooks, J. Delanoe, D. P. Donovan, J. D. Eastment, N. Gaussiat, J. W. F. Goddard, M. Haeffelin, H. Klein Baltink, O. A. Krasnov, J. Pelon, J.-M. Piriou, A. Protat, H. W. J. Russchenberg, A. Seifert, A. M. Tompkins, G.-J. van Zadelhoff, F. Vinit, U. Willen, D. R. Wilson and C. L. Wrench, 2007: Cloudnet: Continuous evaluation of cloud profiles in seven operational models using ground-based observations. *Bull. Amer. Meteor. Soc.*, **88**, 883–898, doi:10.1175/BAMS-88-6-883.

Intrieri, J. M., M. D. Shupe, T. Uttal, and B. J. McCarty, 2002: An annual cycle of Arctic cloud characteristics observed by radar and lidar at SHEBA. *J. Geophys. Res.*, **107**, C10, doi:10.1029/2000JC000423.

Klein, S. A., and D. L. Hartmann, 1993: The seasonal cycle of low stratiform clouds. *J. Clim.*, **6**, 1587–1606.

Kollias, P., and B. Albrecht, 2000: The turbulence structure in a continental stratocumulus cloud from millimeter-wavelength radar observations. *J. Atmos. Sci.*, **57**, 2417–2434.

Kollias, P., B. A. Albrecht, R. Lhermitte, and A. Savtchenko, 2001: Radar observations of updrafts, downdrafts, and turbulence in fair-weather cumuli. *J. Atmos. Sci.*, **58**, 1750–1766.

Kollias, P., E. E. Clothiaux, M. A. Miller, E. P. Luke, K. L. Johnson, K. P. Moran, K. B. Widener, and B. A. Albrecht, 2007a: The Atmospheric Radiation Measurement program cloud profiling radars: Second-generation sampling strategies, processing, and cloud data products. *J. Atmos. Oceanic Technol.*, **24**, 1199–1214, doi:10.1175/JTECH2033.1.

Kollias, P., G. Tselioudis, and B. A. Albrecht, 2007b: Cloud climatology at the Southern Great Plains and the layer structure, drizzle, and atmospheric modes of continental stratus. *J. Geophys. Res.*, **112**, D09116, doi:10.1029/2006JD007307.

Kollias, P., J. Rémillard, E. Luke, and W. Szyrmer, 2011a: Cloud radar Doppler spectra in drizzling stratiform clouds: Part 1. Forward modeling and applications. *J. Geophys. Res.*, **116**, doi:10.1029/2010JD015237.

Kollias, P., W. Szyrmer, J. Rémillard, and E. Luke, 2011b: Cloud radar Doppler spectra in drizzling stratiform clouds: Part 2. Observations and microphysical modeling of

drizzle evolution, *J. Geophys. Res.*, **116**, doi:10.1029/2010JD015238.

Kubar, T. L., D. L. Hartmann, and R. Wood, 2009: Understanding the importance of microphysics and macrophysics for warm rain in marine low clouds. Part I: Satellite observations. *J. Atmos. Sci.*, **66**, 2953–2972.

Kuo, H.-C., and W. H. Schubert, 1988: Stability of cloud-topped boundary layers. *Q. J. R. Meteorol. Soc.*, **114**, 887–916.

Lhermitte, R., 1990: Attenuation and scattering of millimeter wavelength radiation by clouds and precipitation. *J. Atmos. Oceanic Technol.*, **7**, 464–479.

Liljegren, J. C., 1994: Two-channel microwave radiometer for observations of total column precipitable water vapor and cloud liquid water path. Paper presented at the Fifth Symposium on Global Change Studies, Am. Meteorol. Soc., Nashville, Tenn, 262–269.

Liu, Z., M. Vaughan, D. Winker, C. Kittaka, B. Getzewich, R. Kuehn, A. Omar, K. Powell, C. Trepte, and C. Hostetler, 2009: The CALIPSO lidar cloud and aerosol discrimination: Version 2 algorithm and initial assessment of performance. *J. Atmos. Oceanic Technol.*, **26**, 1198–1213, doi:10.1175/2009JTECHA1229.1.

Luke, E. P., P. Kollias, and M. D. Shupe, 2010: Detection of supercooled liquid in mixed-phase clouds using radar Doppler spectra. *J. Geophys. Res.*, **115**, D19201, doi:10.1029/2009JD012884.

Markowicz, K. M., P. J. Flatau, A. E. Kardas, J. Remiszewska, K. Stelmaszczyk, and L. Woeste, 2008: Ceilometer retrieval of the boundary layer vertical aerosol extinction structure. *J. Atmos. Oceanic Technol.*, **25**, 928–944, doi:10.1175/2007JTECHA1016.1.

Mead, J. B., and K. B. Widener, 2005: W-band ARM cloud radar. Preprints. *32nd Int.*

Conf. on Radar Meteorology, Albuquerque, NM, Amer. Meteor. Soc., CD-ROM, P1R.3.

Münkel, C., N. Eresmaa, J. Räsänen, and A. Karppinen, 2007: Retrieval of mixing height and dust concentration with lidar ceilometer. *Bound.-Layer Meteor.*, **124**, 117–128.

Nicholls, S., 1989: The structure of radiatively driven convection in stratocumulus. *Q. J. R. Meteorol. Soc.*, **115**, 487–511.

Norris, J. R., and S. A. Klein, 2000: Low cloud type over the ocean from surface observations. Part III: Relationship to vertical motion and the regional surface synoptic environment. *J. Clim.*, **13**, 245–256.

O'Connor, E. J., R. J. Hogan, and A. J. Illingworth, 2005: Retrieving stratocumulus drizzle parameters using Doppler radar and lidar. *J. Appl. Meteorol.*, **44**, 14–27.

Ramanathan, V., R. D. Cess, E. F. Harrison, P. Minnis, B. R. Barkstrom, E. Ahmad, and D. Hartmann, 1989: Cloud-radiative forcing and climate: Results from the Earth Radiation Budget Experiment. *Science*, **243**, 57–63.

Randall, D. A., J. A. Coakley Jr., D. H. Lenschow, C. W. Fairall, and R. A. Kropfli, 1984: Outlook for research on subtropical marine stratiform clouds. *Bull. Amer. Meteor. Soc.*, **65**, 1290–1301.

Randall, D. A., Q. Shao, and C.-H. Moeng, 1992: A second-order bulk boundary-layer model. *J. Atmos. Sci.*, **49**, 1903–1923.

Rozendaal, M. A., C. B. Leovy, and S. A. Klein, 1995: An observational study of diurnal variations of marine stratiform cloud. *J. Clim.*, **8**, 1795–1809.

Serpetzoglou, E., B. A. Albrecht, P. Kollias, and C. W. Fairall, 2008: Boundary layer,

cloud, and drizzle variability in the southeast Pacific stratocumulus regime. *J. Clim.*, **21**, 6191–6214.

Stevens, B., D. H. Lenschow, G. Vali, H. Gerber, A. Bandy, B. Blomquist, J.-L. Brenguier, C. S. Bretherton, F. Burnet, T. Campos, S. Chai, I. Faloona, D. Friesen, S. Haimov, K. Laursen, D. K. Lilly, S. M. Loehrer, S. P. Malinowski, B. Morley, M. D. Petters, D. C. Rogers, L. Russell, V. Savic-Jovcic, J. R. Snider, D. Straub, M. J. Szumowski, H. Takagi, D. C. Thornton, M. Tschudi, C. Twohy, M. Wetzel, and M. C. van Zanten, 2003: Dynamics and chemistry of marine stratocumulus—DYCOMS-II. *Bull. Amer. Meteor. Soc.*, **84**, 579–593, doi:10.1175/BAMS-84-5-579.

Ulaby, F. T., R. K. Moore, and A. K. Fung, 1981: *Microwave remote sensing: Active and passive. Vol. 1, Microwave remote sensing fundamentals and radiometry*, Addison-Wesley, 456 pp.

Wang, J., and W. B. Rossow, 1995: Determination of cloud vertical structure from upper-air observations. *J. Appl. Meteorol.*, **34**, 2243–2258.

Wood, R., 2005: Drizzle in stratiform boundary layer clouds. Part I: Vertical and horizontal structure. *J. Atmos. Sci.*, **62**, 3011–3033.

Wood, R, and C. S. Bretherton, 2004: Boundary layer depth, entrainment, and decoupling in the cloud-capped subtropical and tropical marine boundary layer. *J. Clim.*, **17**, 3576–3588.

Wood, R, and C. S. Bretherton, 2006: On the relationship between stratiform low cloud cover and lower tropospheric stability. *J. Clim.*, **19**, 6425–6432.

Wood, R., C. S. Bretherton, and D. L. Hartmann, 2002: Diurnal cycle of liquid water path over the subtropical and tropical oceans. *Geophys. Res. Lett.*, **29**, 2092, doi:10.1029/2002GL015371.

Wood, R., C. R. Mechoso, C. S. Bretherton, R. A. Weller, B. Huebert, F. Straneo, B. A. Albrecht, H. Coe, G. Allen, G. Vaughan, P. Daum, C. Fairall, D. Chand, L. Gallardo Klenner, R. Garreaud, C. Grados, D. S. Covert, T. S. Bates, R. Krejci, L. M. Russell, S. de Szoeke, A. Brewer, S. E. Yuter, S. R. Springston, A. Chaigneau, T. Toniazzo, P. Minnis, R. Palikonda, S. J. Abel, W. O. J. Brown, S. Williams, J. Fochesatto, J. Brioude, and K. N. Bower, 2011: The VAMOS Ocean-Cloud-Atmosphere-Land Study Regional Experiment (VOCALS-REx): goals, platforms, and field operations. *Atmos. Chem. Phys.*, **11**, 627–654, doi:10.5194/acp-11-627-2011.

Yin, B., and B. A. Albrecht, 2000: Spatial variability of atmospheric boundary layer structure over the eastern equatorial Pacific. *J. Clim.*, **13**, 1574–1592.

Zhang, G. J., A. M. Vogelmann, M. P. Jensen, W. D. Collins, and E. P. Luke, 2010: Relating satellite-observed cloud properties from MODIS to meteorological conditions for marine boundary layer clouds. *J. Clim.*, **23**, 1374–1391, doi:10.1175/2009JCLI2897.1.

Zuidema, P., E. R. Westwater, C. Fairall, and D. Hazen, 2005: Ship-based liquid water path estimates in marine stratocumulus. *J. Geophys. Res.*, **110**, D20206, doi:10.1029/2005JD005833.

7. FIGURE CAPTION

Fig. 1 Monthly statistics of good running time for the WACR (black), ceilometer (dark gray), and MWR (light gray). Operations are considered bad when more than a minute separates successive measurements. Note that the radar started working in early June 2009, and it was down for about 23 days in September 2010. Note also that the radiometer measurements from July 11, 2010 through August 9, 2010 are unreliable, due to a software problem, although it is not shown here. The numbers above the graph represent the number of soundings taken during each month that returned good measurements.

Fig. 2 Top: True color images from MODIS on board Terra taken around 1315UTC, and span about 500km on both dimensions centered on the location of Graciosa Island (shown in red circle). The left image shows a stratocumulus cloud case (November 22, 2009) and the right image shows a broken cumulus case (August 30, 2010). Bottom: The corresponding daily WACR time-height reflectivity observations with the first ceilometer cloud base shown in black dots.

Fig. 3 Monthly statistics of (a) cloud and liquid precipitation coverage using the lidar-radar algorithm, (b) the four main cloud types, (c) low-level clouds, and (d) liquid precipitation types. Note that the September 2010 results come from only 8 days due to a radar downtime. Note also that the precipitation reported here relates to the first cloud layer only. (e) Time series of LTS as retrieved from the radiosondes launches.

Fig. 4 a) Distributions of the hourly cloud base heights for the stratocumulus and cumulus clouds (respectively the black and gray lines). b) Distributions of the distance between the transition layer and the cumulus hourly base (gray line), and between the stratocumulus hourly top and the inversion layer (black line).

Fig. 5 Monthly statistics of (a) the transition and inversion layers base height, and the stratocumulus clouds boundaries, and (b) the occurrences of the inversion and transition layers, as a fraction of the number of soundings per month.

Fig. 6 Daily (a) and annual (b) cycles of hours characterized by single and multi-layer clouds in the MBL (respectively the gray and black bars). Each number of occurrences is normalized by the total number of hours with data within the considered hour (a) or month (b), to provide percentage values. Note that the local standard time in Azores is UTC-1h.

Fig. 7 Profiles of (a) potential temperature (black; bottom axis) and water vapor mixing ratio (gray; top axis), (b) wind speed, (c) wind direction, and (d) relative humidity composited over the cases with multiple BL clouds (dash-dotted lines), a single BL cloud at the inversion or transition level (solid and dashed lines respectively), all presenting a transition layer.

Fig. 8 Distribution of instantaneous cloud base (a) and depth (b), LWP (c), inversion depth (d) and strengths (e), and transition strength (f) measured in the selected stratocumulus cases. In (a)-(c), measurements were divided according to the absence or presence of a drizzle shaft (respectively the black and gray curves). In (e), the strength is reported in terms of equivalent potential temperature (black curve), and in terms of water vapor mixing ratio (gray curve). In (f), the vertical dashed line corresponds to the minimum value used to detect a transition layer (based on Yin and Albrecht, 2000).

Fig. 9 3-hourly statistics, composited from 35 days of persisting single-layer stratocumulus coverage, separated between periods without radar echoes below the cloud base and periods with various types of drizzle (virga, shallow, or intense): (a) fraction of the stratocumulus coverage, (b) cloud base (dashed) and top (solid) heights, (c) cloud depth, and (d) LWP from the MWR. The average stratocumulus coverage is also included in (a) with the thick line.

Fig. 10 Night (solid) and day (dashed) average profiles of the hourly-estimated variance and skewness of the radar measured mean Doppler velocity (a and c respectively), and 3-hourly profiles of the variance and skewness of the radar measured mean Doppler velocity (b and d respectively), composited over the selected periods of stratocumulus without drizzle under the cloud base. Note that the vertical axis represents the height above cloud base, in units of cloud depths, thus covering only the cloud layer.

Fig. 11 Night (black) and day (gray) profiles of (a) updraft and downdraft velocities, (b) updraft area, and (c) mass flux associated with the updrafts, as obtained using three methods: direct sampling (solid lines), coherent structures only (short dashes), and the statistical method (long dashes).

Table 1a: List of liquid precipitation types and their main characteristics used to differentiate them.

Type	Virga	Light	Intense
Echo base	> 200m	< 200m	< 200m
Base reflectivity	—	< 0dBZ	≥ 0dBZ
Echo below CB	Yes	Yes	Possible

Table 1b: List of cloud types and their main characteristics used to differentiate them in the identification algorithm. The last row indicates the type of precipitation most likely associated with each cloud type.

Type → Characteristic ↓	High	Middle	Low			Deep BL
			Cu	Sc	conv	
Cloud base	> 7km	> 3km	—	—	—	≤ 3km
Cloud top	—	—	≤ 3km	≤ 3km	≤ 3km	> 3km
Duration	—	—	< 20min	≥ 20min	≥ 20min	—
CT variability	—	—	—	< 100m	≥ 100m	—
Type of precip	—	virga	virga	light	intense	intense

Table 2: List of the selected stratocumulus cases, with some observed properties averaged throughout the considered period: the cloud base and top mean height (and standard deviation), the daily coverage of drizzle and cloud, the mean LWP, the mean criterion for the presence of a transition layer, the mean strength of the inversion layer in potential temperature and mixing ratio ($\Delta X = X_{top} - X_{base}$), and the possible air mass origin as obtained using HYSPLIT (E-Coast: North America East Coast; N-Can: Northern Canada; N-Eur: Northern Europe).

Day [y/m/d]	Cloud base [m]	Cloud top [m]	Drizzle / Cloud [%]	LWP [g/m^2]	$\frac{\mu_{max}}{\overline{\mu}}$	Inversion		Air mass origin
						$\Delta\theta$ [K]	Δr [g/kg]	
09/06/22	1447 ± 344	1915 ± 117	35 / 52	167	—	—	—	Marine
09/07/29	1203 ± 195	1485 ± 152	49 / 77	86	3.66	4.7	-4.7	E-Coast
09/08/08	446 ± 240	929 ± 267	45 / 74	160	3.17	3.6	-3.4	Marine
09/08/12	1185 ± 114	1435 ± 64	43 / 57	109	4.66	6.8	-6.0	E-Coast
09/09/13	761 ± 282	1377 ± 190	44 / 51	165	8.72	4.3	-7.2	N-Can
09/11/02	1012 ± 63	1143 ± 66	10 / 59	18	8.63	9.0	-6.0	N-Can
09/11/03	680 ± 231	1069 ± 312	46 / 72	80	-15.2	5.5	-2.4	Marine
09/11/07	340 ± 110	616 ± 152	49 / 75	101	2.33	6.1	-3.8	Marine
09/11/22	1345 ± 99	1600 ± 76	88 / 98	80	13.1	7.2	-4.2	W-Coast
09/11/23	1533 ± 190	1751 ± 144	46 / 68	64	7.61	6.4	-4.8	Prairies
09/11/29	1567 ± 205	1880 ± 97	69 / 86	88	7.27	8.1	-5.0	Marine
10/01/28	1160 ± 225	1587 ± 143	54 / 58	140	5.35	8.9	-4.0	N-Eur
10/01/29	1365 ± 234	1719 ± 144	79 / 90	107	5.23	8.1	-3.6	N-Eur
10/01/31	1182 ± 126	1384 ± 89	43 / 73	43	10.2	6.7	-3.2	Marine
10/04/13	1416 ± 265	1806 ± 131	80 / 99	133	8.46	7.7	-3.6	N-Eur
10/05/11	1410 ± 320	1779 ± 246	65 / 79	116	4.33	7.1	-2.7	Marine
10/05/12	1460 ± 357	1870 ± 237	58 / 72	139	4.82	6.0	-3.3	Marine
10/06/06	645 ± 253	1086 ± 138	51 / 67	133	4.14	4.6	-3.7	Marine
10/06/07	582 ± 147	881 ± 71	34 / 60	66	11.8	6.8	-6.1	Marine
10/06/13	905 ± 41	1128 ± 59	3 / 60	55	14.9	7.6	-4.3	Arctic
10/06/15	895 ± 143	1147 ± 137	35 / 64	91	0.085	5.0	-3.9	Marine
10/06/16	1024 ± 85	1204 ± 85	13 / 66	35	2.94	7.8	-5.1	Marine
10/06/22	903 ± 109	1197 ± 82	46 / 50	97	12.0	7.2	-4.2	E-Coast
10/07/06	737 ± 93	1034 ± 81	76 / 85	117	3.84	4.8	-3.2	Marine
10/07/07	696 ± 201	1105 ± 165	71 / 83	152	4.08	6.3	-4.3	Marine
10/07/13	309 ± 165	659 ± 88	21 / 67	—	3.69	4.4	-4.9	Marine
10/07/29	1234 ± 146	1495 ± 76	44 / 82	—	3.80	8.0	-5.6	Marine
10/07/31	1122 ± 319	1518 ± 64	47 / 91	—	3.97	7.7	-5.5	Marine
10/10/03	901 ± 179	1246 ± 154	75 / 95	74	4.43	5.4	-4.3	E-Coast
10/10/04	1018 ± 207	1313 ± 271	23 / 51	51	3.54	4.7	-3.2	Marine
10/10/11	585 ± 130	932 ± 94	64 / 74	84	5.32	4.7	-4.3	Marine
10/10/12	771 ± 202	1204 ± 245	64 / 72	71	3.35	6.0	-4.7	E-Can
10/11/07	1048 ± 158	1402 ± 96	62 / 67	92	11.3	7.6	-4.0	Arctic
10/11/08	834 ± 73	1140 ± 54	70 /100	62	6.29	10.7	-5.2	Arctic
10/11/14	1458 ± 126	1803 ± 114	65 / 73	103	9.42	9.8	-4.0	Marine

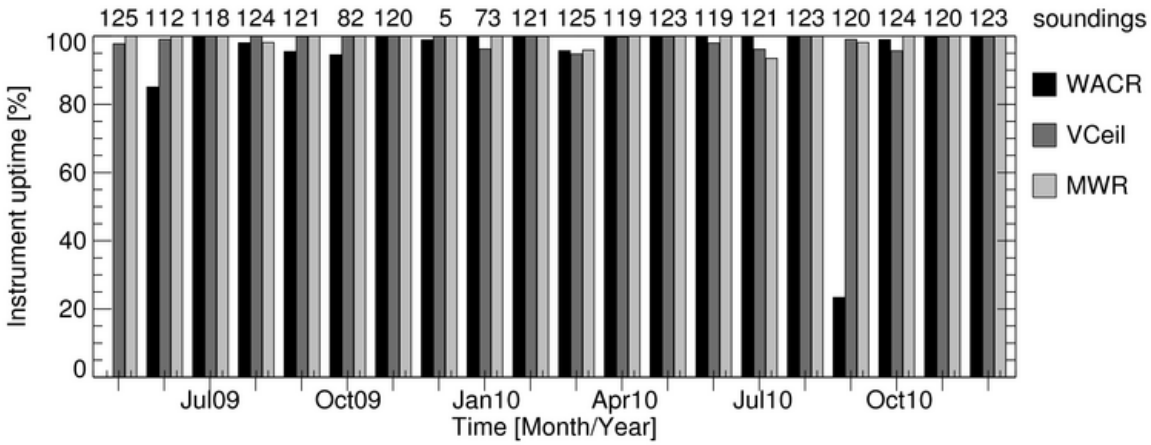

Fig. 1 Monthly statistics of good running time for the WACR (black), ceilometer (dark gray), and MWR (light gray). Operations are considered bad when more than a minute separates successive measurements. Note that the radar started working in early June 2009, and it was down for about 23 days in September 2010. Note also that the radiometer measurements from July 11, 2010 through August 9, 2010 are unreliable, due to a software problem, although it is not shown here. The numbers above the graph represent the number of soundings taken during each month that returned good measurements.

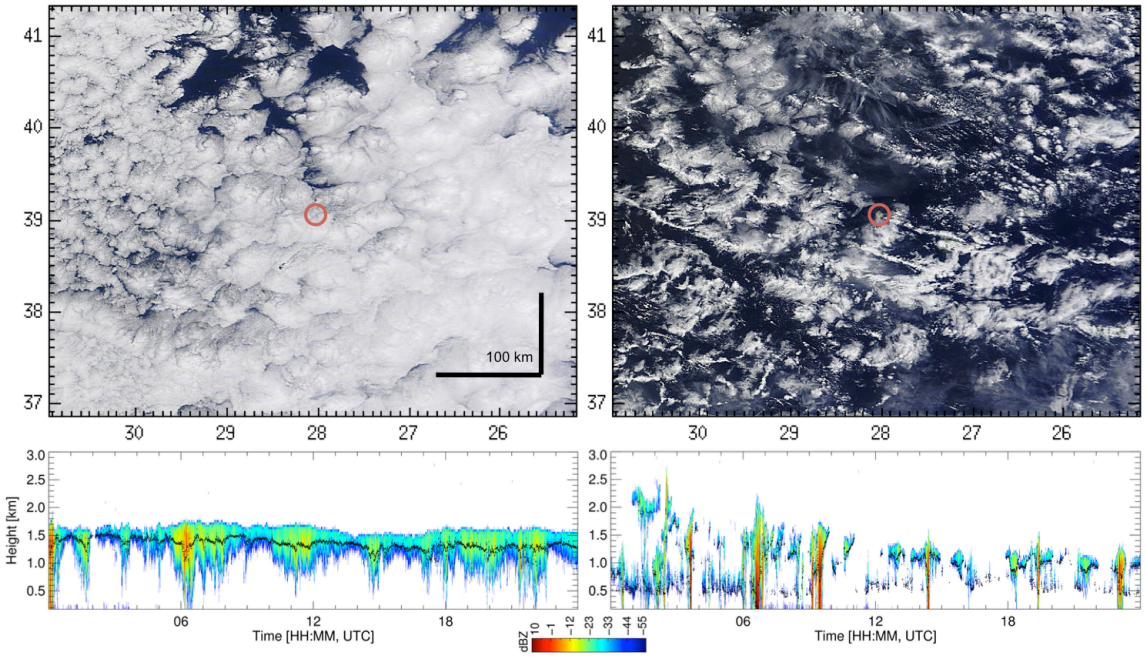

Fig. 2 Top: True color images from MODIS on board Terra taken around 1315UTC, and span about 500km on both dimensions centered on the location of Graciosa Island (shown in red circle). The left image shows a stratocumulus cloud case (November 22, 2009) and the right image shows a broken cumulus case (August 30, 2010). Bottom: The corresponding daily WACR time-height reflectivity observations with the first ceilometer cloud base shown in black dots

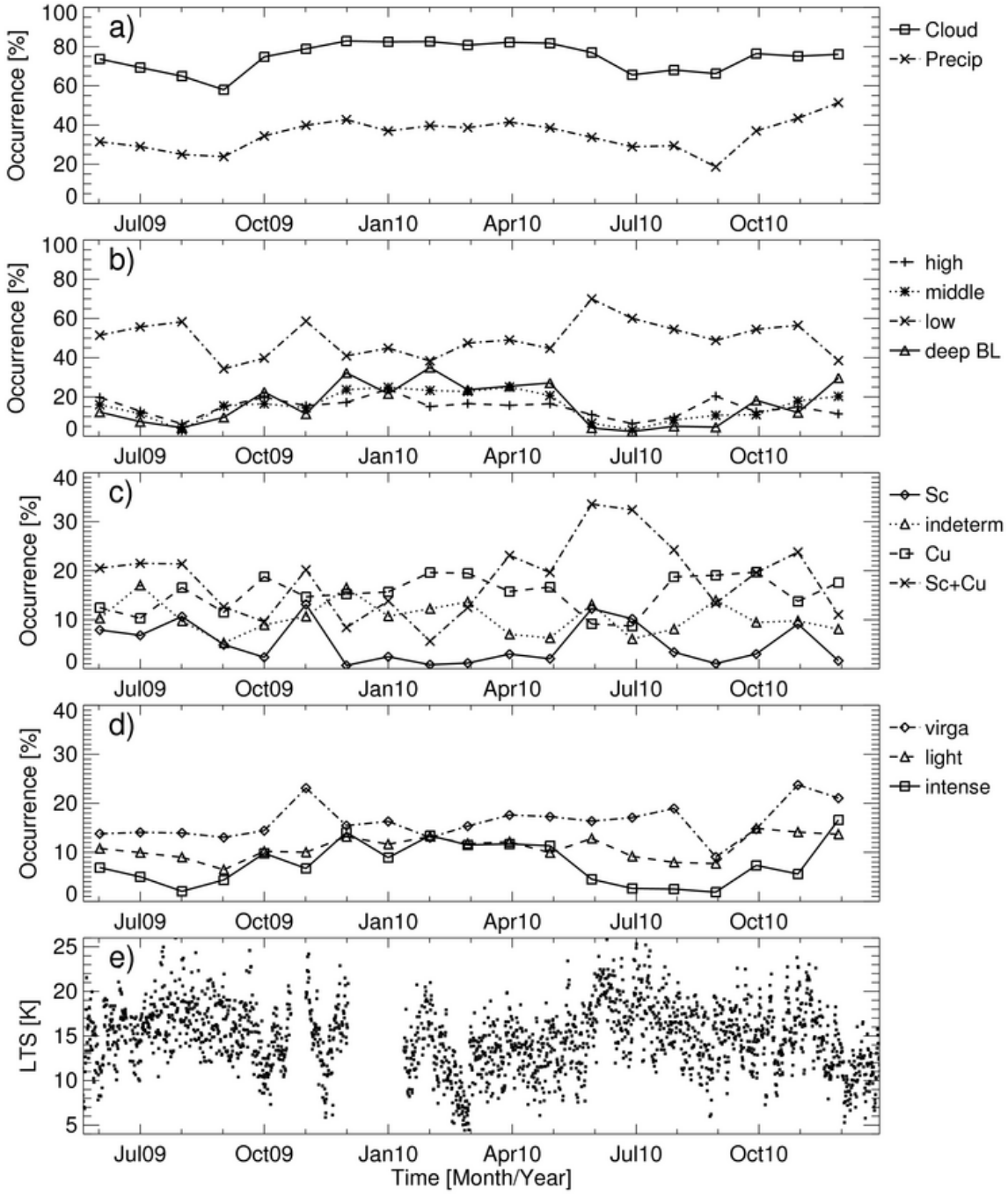

Fig. 3 Monthly statistics of (a) cloud and liquid precipitation coverage using the lidar-radar algorithm, (b) the four main cloud types, (c) low-level clouds, and (d) liquid precipitation types. Note that the September 2010 results come from only 8 days due to a radar downtime. Note also that the precipitation reported here relates to the first cloud layer only. (e) Time series of LTS as retrieved from the radiosondes launches.

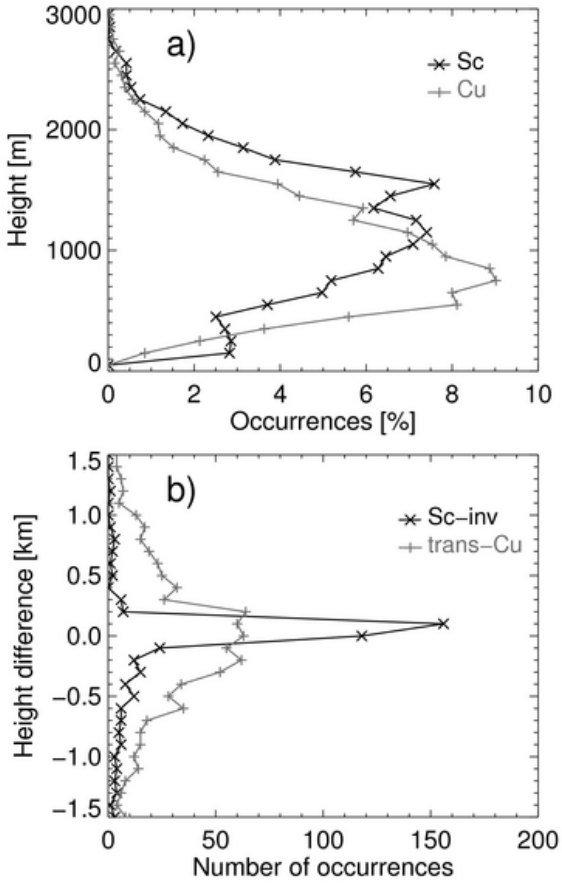

Fig. 4 a) Distributions of the hourly cloud base heights for the stratocumulus and cumulus clouds (respectively the black and gray lines). b) Distributions of the distance between the transition layer and the cumulus hourly base (gray line), and between the stratocumulus hourly top and the inversion layer (black line).

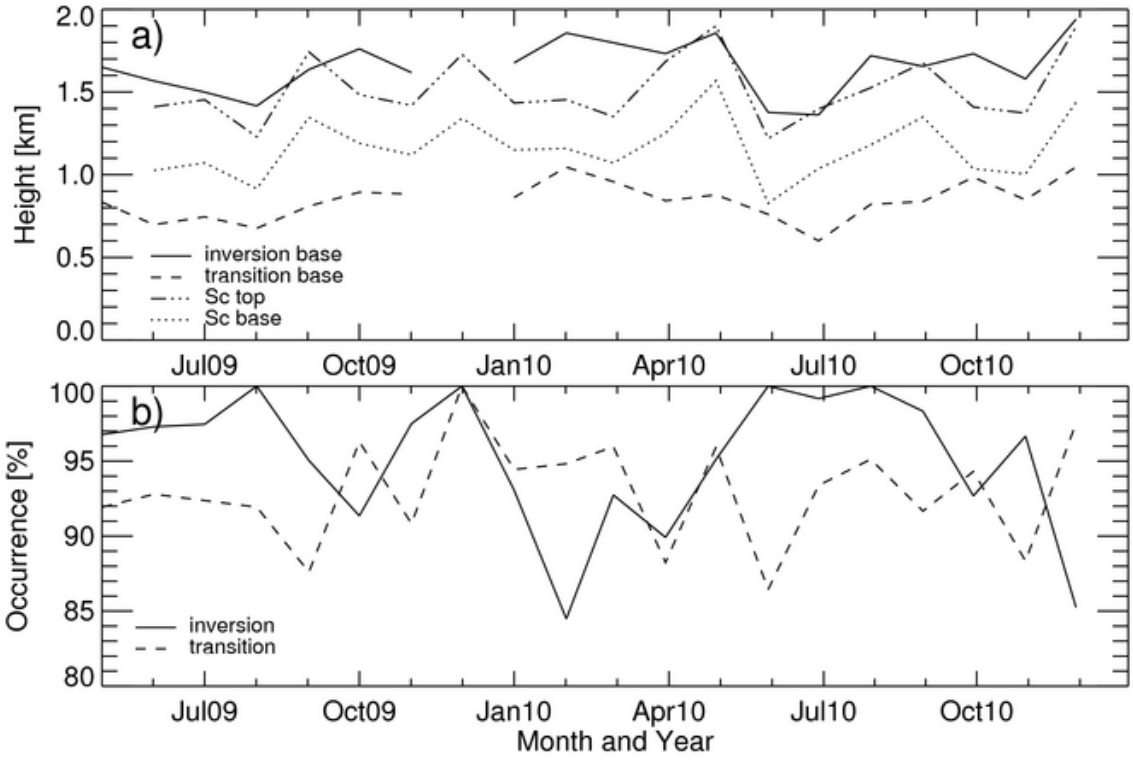

Fig. 5 Monthly statistics of (a) the transition and inversion layers base height, and the stratocumulus clouds boundaries, and (b) the occurrences of the inversion and transition layers, as a fraction of the number of soundings per month.

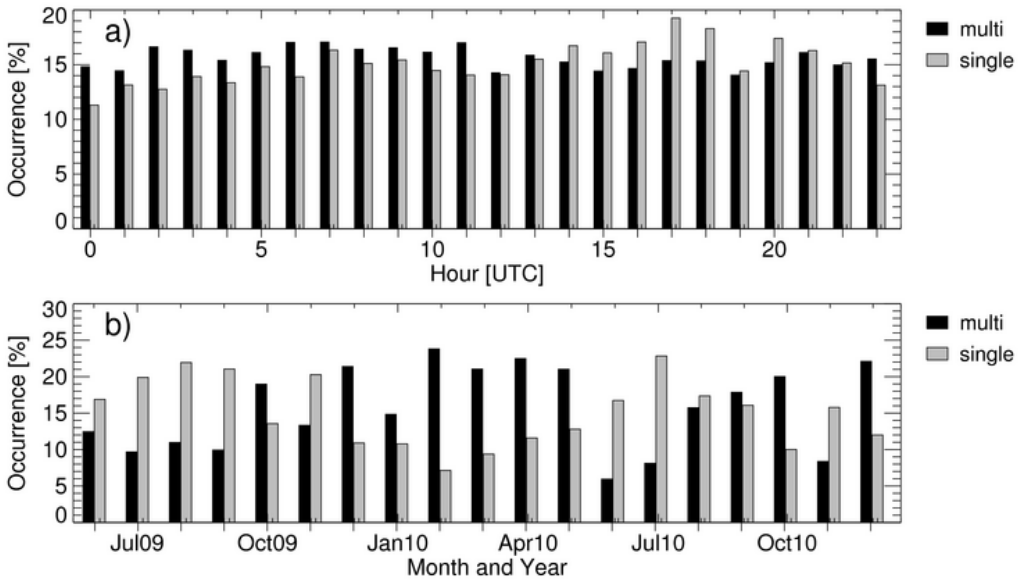

Fig. 6 Daily (a) and annual (b) cycles of hours characterized by single and multi-layer clouds in the MBL (respectively the gray and black bars). Each number of occurrences is normalized by the total number of hours with data within the considered hour (a) or month (b), to provide percentage values. Note that the local standard time in Azores is UTC-1h.

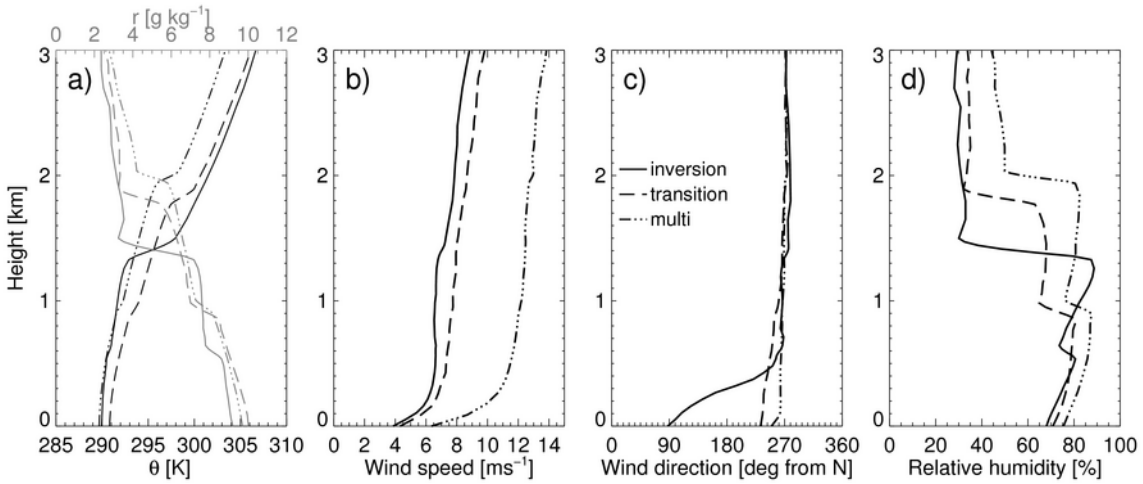

Fig. 7 Profiles of (a) potential temperature (black; bottom axis) and water vapor mixing ratio (gray; top axis), (b) wind speed, (c) wind direction, and (d) relative humidity composited over the cases with multiple BL clouds (dash-dotted lines), a single BL cloud at the inversion or transition level (solid and dashed lines respectively), all presenting a transition layer.

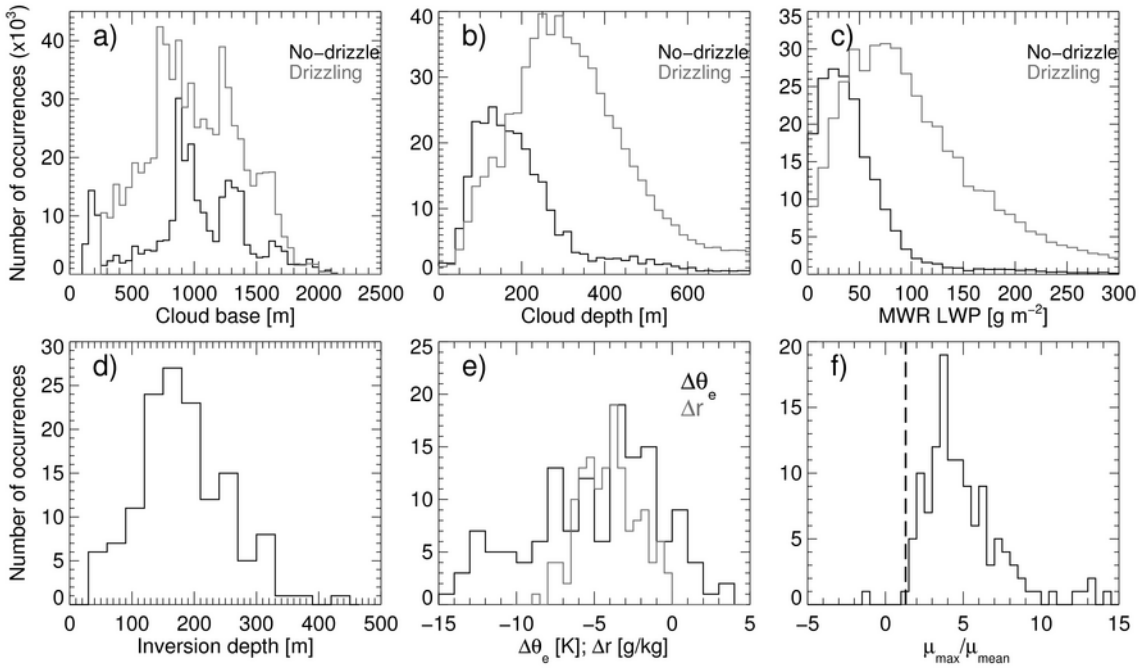

Fig. 8 Distribution of instantaneous cloud base (a) and depth (b), LWP (c), inversion depth (d) and strengths (e), and transition strength (f) measured in the selected stratocumulus cases. In (a)-(c), measurements were divided according to the absence or presence of a drizzle shaft (respectively the black and gray curves). In (e), the strength is reported in terms of equivalent potential temperature (black curve), and in terms of water vapor mixing ratio (gray curve). In (f), the vertical dashed line corresponds to the minimum value used to detect a transition layer (based on Yin and Albrecht, 2000).

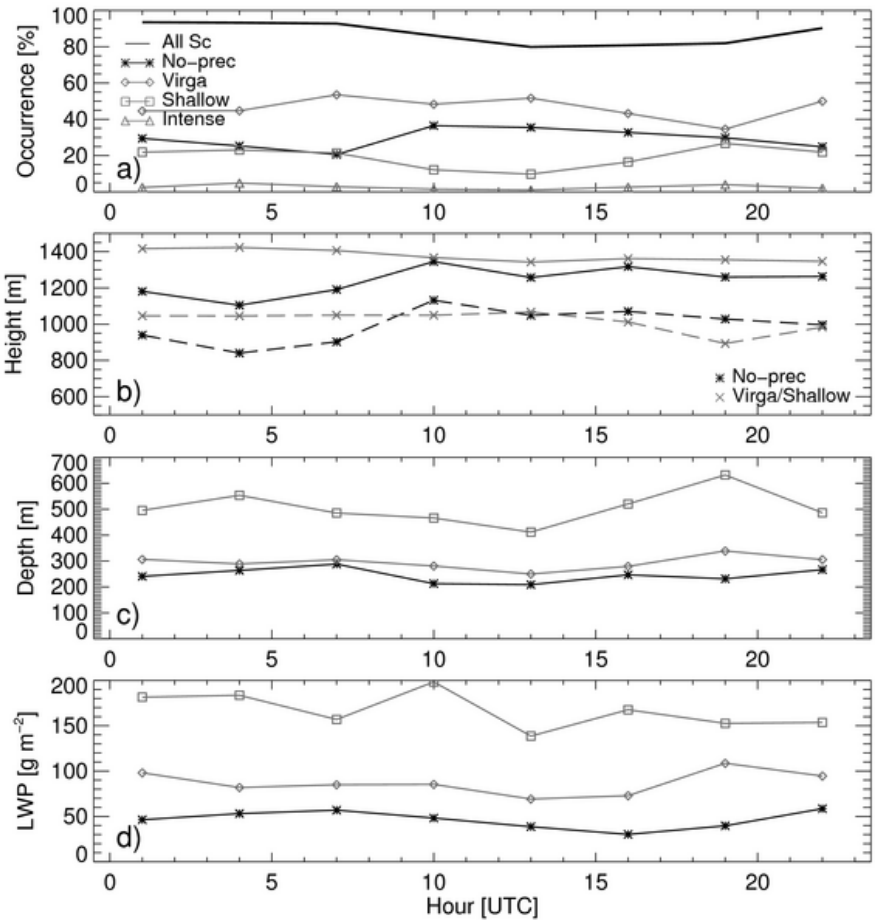

Fig. 9 3-hourly statistics, composited from 35 days of persisting single-layer stratocumulus coverage, separated between periods without radar echoes below the cloud base and periods with various types of drizzle (virga, shallow, or intense): (a) fraction of the stratocumulus coverage, (b) cloud base (dashed) and top (solid) heights, (c) cloud depth, and (d) LWP from the MWR. The average stratocumulus coverage is also included in (a) with the thick line.

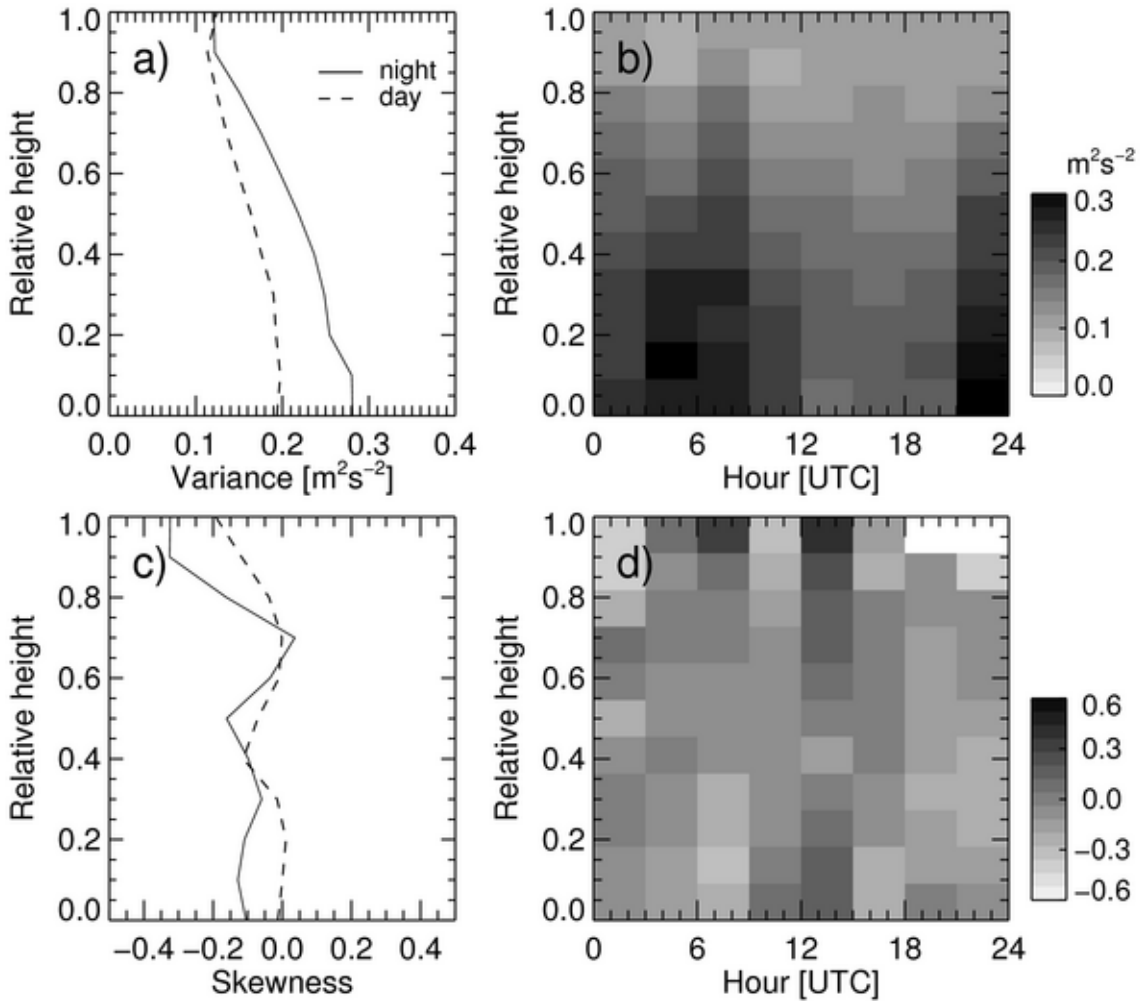

Fig. 10 Night (solid) and day (dashed) average profiles of the hourly-estimated variance and skewness of the radar measured mean Doppler velocity (a and c respectively), and 3-hourly profiles of the variance and skewness of the radar measured mean Doppler velocity (b and d respectively), composited over the selected periods of stratocumulus without drizzle under the cloud base. Note that the vertical axis represents the height above cloud base, in units of cloud depths, thus covering only the cloud layer.

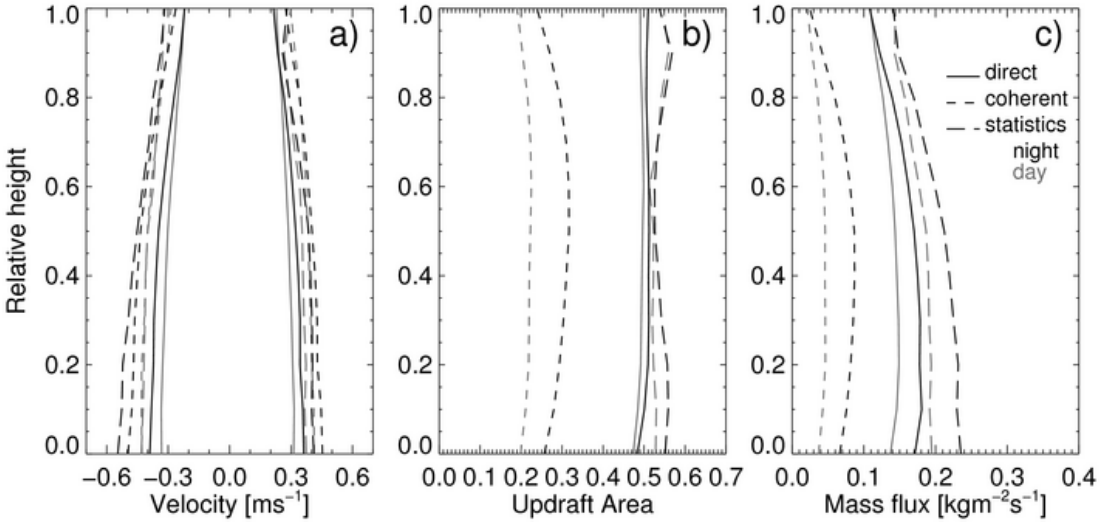

Fig. 11 Night (black) and day (gray) profiles of (a) updraft and downdraft velocities, (b) updraft area, and (c) mass flux associated with the updrafts, as obtained using three methods: direct sampling (solid lines), coherent structures only (short dashes), and the statistical method (long dashes).